PURPOSE-LED PUBLISHING™

PAPER

Secondary electron emission current mapping for nanoscale thermometry

To cite this article: William A Hubbard *et al* 2025 *Nanotechnology* **36** 265704

View the article online for updates and enhancements.

You may also like

- Effect of rough surface morphology on secondary electron emission from metal surface
Na Zhang, Meng Cao, Wan-Zhao Cui et al.
- Carbon-Coated Porous Aluminum Oxides Used as Spacer Overlayers to Reduce Secondary Electron Emission for Field Emission Display Applications
Tung-Yuan Yu, Fu-Ming Pan, Cheng-Li Chen et al.
- A synthetic semi-empirical physical model of secondary electron yield of metals under *E*-beam irradiation
Guo-Bao Feng, , Wan-Zhao Cui et al.

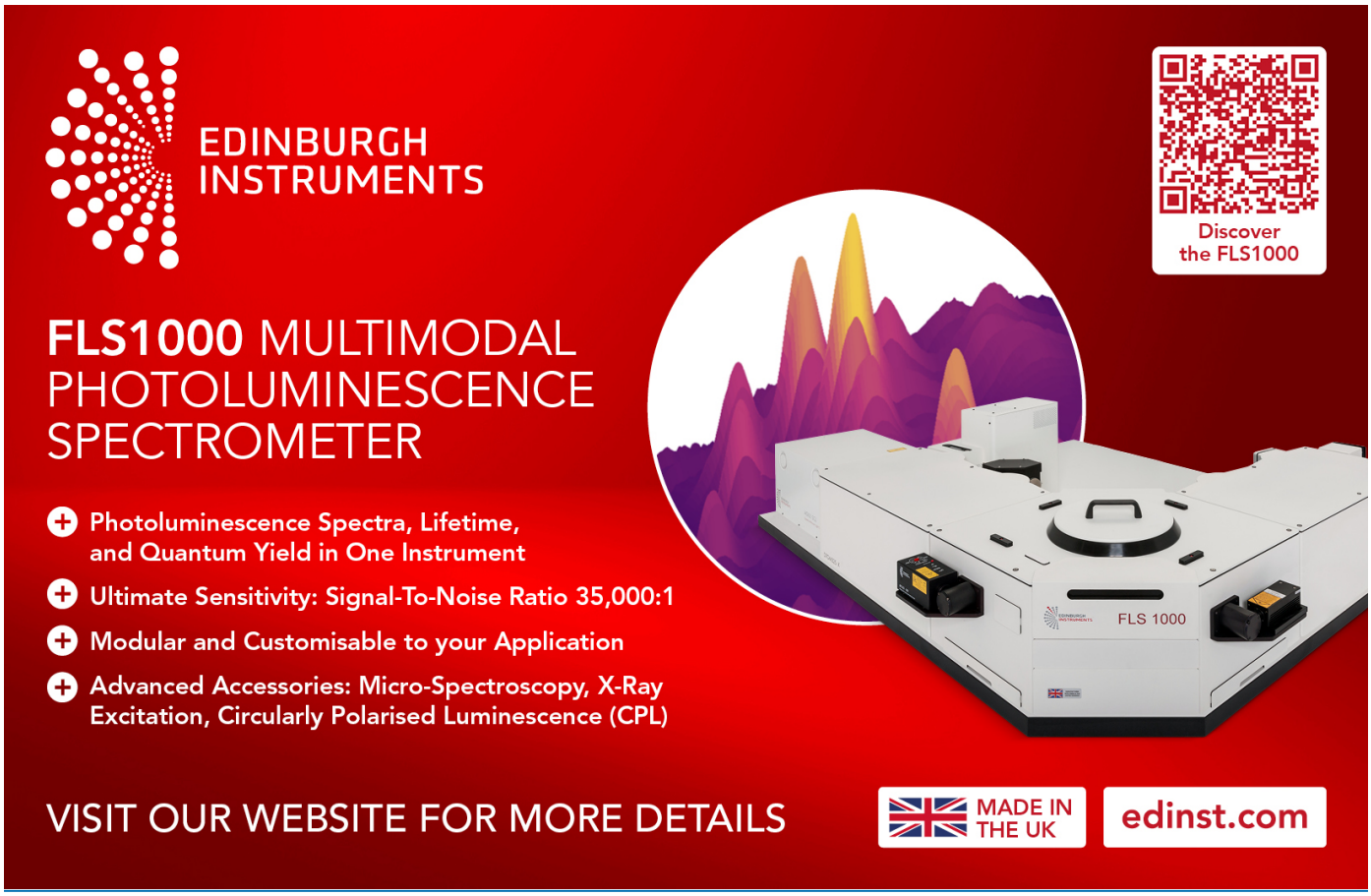

This content was downloaded from IP address 128.138.140.254 on 03/09/2025 at 21:40

IOP Publishing Nanotechnology
Nanotechnology **36** (2025) 265704 (7pp) https://doi.org/10.1088/1361-6528/ade445

Secondary electron emission current mapping for nanoscale thermometry

William A Hubbard[1,*], **Matthew Mecklenburg**[2], **Ho Leung Chan**[2,3] and **B C Regan**[1,2,3]

[1] NanoElectronic Imaging, Riverside, CA 92506, United States of America
[2] California NanoSystems Institute, University of California, Los Angeles, CA 90095, United States of America
[3] Department of Physics and Astronomy, University of California, Los Angeles, CA 90095, United States of America

E-mail: bhubbard@NanoElectronicImaging.com

Received 1 April 2025, revised 5 June 2025
Accepted for publication 13 June 2025
Published 24 June 2025

Abstract

Secondary electron (SE) emission is temperature-dependent, and thus could form the basis of an electron microscopy-based thermometry technique with nanoscale spatial resolution. To explore this possibility, we measure the SE emission from heated test structures using scanning transmission electron microscopy electron beam-induced current (STEM EBIC) imaging. The test structures consist of an electrode, which is made of platinum or amorphous carbon, and an encircling heater. Aluminium nanoparticles decorate the test structures and serve as local nanothermometers that we read-out with plasmon energy expansion themometry (PEET). Energizing the heaters, we measure the SE emission from the electrodes and nanothermometers. The SE emission from Pt, C, and Al is a simple, supralinear function of the PEET-calibrated temperature that is well-fit with a single free parameter. SEEBIC thermometry thus shows promise for being a widely applicable, TEM-based temperature mapping technique.

Supplementary material for this article is available online

Keywords: TEM, thermometry, STEM EBIC, high-resolution

1. Introduction

Irradiating a material with a high-energy electron beam causes lower energy ($\leqslant$50 eV) 'secondary' electrons (SEs) to be emitted. SE emission has been studied extensively due to its role as one of the main imaging signals in the scanning electron microscope (SEM). The emission of SEs at a given beam position is most often measured by an off-sample detector. The SE signal detected in the SEM typically includes contributions from SEs emitted by the primary beam, SE1, and by backscattered electrons (BSEs), SE2 [1]. In the SEM, SE2 will generally be a large, if not dominant, portion of the total SEs emitted [1, 2]. The superposition of SE1 and SE2 makes quantitative analysis of SE signal challenging, and the larger interaction volume associated with BSEs, and therefore SE2, contributes to the resolution limit of SE imaging in SEM.

In the transmission electron microscope (TEM), samples are generally thinner (<150 nm) and the primary electron energies are larger ($\geqslant$60 keV) compared to SEM. As a result, in TEM there is a negligible amount BSEs [3, 4], and therefore SE2, and only SE1 emission is expected [5]. The

* Author to whom any correspondence should be addressed.

© 2025 IOP Publishing Ltd. All rights, including for text and data mining, AI training, and similar technologies, are reserved.

interaction volume associated with SEs in TEM is therefore much smaller than in SEM, and even small enough to allow atomic-resolution SE imaging in a scanning TEM (STEM) [6–9].

SE imaging in STEM is typically performed using a SE detector like those used in SEM [6–8], but SE's can also be detected via the holes they leave behind. In SE emission electron beam-induced current (SEEBIC) imaging [4, 10], the current of SEs (or, more precisely, the SE1 current) leaving the sample is measured directly. Unlike the standard, electron–hole pair separation-based mode of EBIC imaging [11], SEEBIC has been demonstrated only in STEM, requires no electric field to generate contrast, and can achieve atomic resolution [9, 12]. Quantitative SEEBIC imaging can map electronic properties such as local conductivity [13–15] and work function [4], and SEEBIC can also assist is resolving 3D nanostructures [16–18].

In this article we demonstrate that SEEBIC imaging can be used to perform quantitative temperature mapping in the TEM. The temperature dependence of SE emission and its promise as the basis for a thermometry technique have been investigated previously. While SE emission is expected to increase with temperature [19, 20], in the SEM the opposite effect was observed [21]. The decrease in SE emission with increased temperature may be due to the various, non-SE1 contributions to the SE signal [1, 22] that are typically absent in SEEBIC.

In the past decade, a number of specialized techniques have been developed to measure temperature in the TEM [23–27]. In each of these methods, temperature is extracted by measuring one of the specimen's physical properties, such as its density, lattice spacing, or phonon spectrum. The first of these techniques reported, and to date the only to demonstrate temperature mapping (rather than single-point measurements), is plasmon energy expansion thermometry (PEET) [23, 28]. In PEET, electron energy loss spectroscopy (EELS) is used to measure a material's plasmon energy. Because the plasmon energy depends on the material's physical density, precision measurements of the plasmon energy can be converted into temperature measurements via the material's independently-determined coefficient of thermal expansion. Performing this analysis and conversion at each pixel in an EELS spectrum image produces a temperature map.

PEET works best in materials with sharp plasmon resonances. Aluminum [23, 29, 30] and indium [31], for instance, are particularly good. Silicon [32], silicon nitride [33], and MoS_2 [34, 35] are serviceable, while other materials are only suitable for detecting large temperature shifts [36, 37]. However, PEET is not generally applicable because not all materials have well-defined plasmon resonances, and because sometimes other sources of density changes (e.g. strain) [38] and, to some extent, sample thickness [23, 39] in a specimen confuse the picture. In the experiments described below, we use PEET on Al nanoparticles to measure local temperature as a calibration for SEEBIC-based temperature measurements [29].

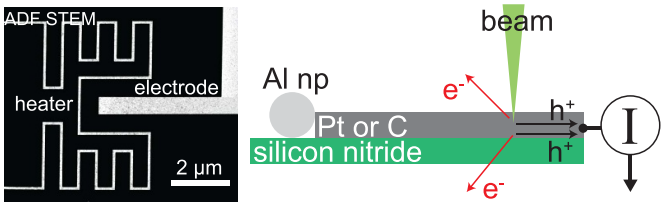

Figure 1. *Left* ADF STEM image of a test structure with a Pt heater and a Pt electrode. In some devices the latter is not Pt but amorphous carbon. *Right* Cartoon side view of an electrode and SE emission, with the current meter measuring the resulting holes.

2. Methods

2.1. Sample preparation

Using a process described previously [4], devices are fabricated on thin Si_3N_4 membrane windows supported by silicon substrates. Optical lithography and electron beam evaporation is used to pattern Ti/Pt (5/25 nm) probe pads and traces that reach the edges of the membrane windows [4]. Ti/Pt (5/25 nm) heaters contacting two of the traces are then patterned on the membrane window via electron beam lithography and evaporation. The Ti/Pt layer thicknesses are chosen to maintain high-electron-transparency without significantly compromising device robustness. Either a Ti/Pt electrode, contacting a third trace, is deposited simultaneously with the heater (figure 1, left), or a 30 nm-thick amorphous carbon (a-C) electrode is patterned with an additional round of electron beam lithography and evaporation. For brevity, we will refer to these device architectures, respectively, as being 'platinum' or 'carbon', despite the former having a 5 nm Ti adhesion layer [4] and both electrodes being supported by Si_3N_4. Aluminum nanoparticles, sourced commercially from SkySpring Nanomaterials, are suspended in isopropanol using sonication and drop-cast onto completed devices to act as PEET nanothermometers. To eliminate beam-induced contamination (Supplementary Data, figure S1), samples are cleaned for 10 s in Ar/H_2 plasma using a Gatan Solarus 950 before they are inserted into the TEM. Optical and then STEM imaging is used to identify samples with suitable nanoparticle thermometers.

2.2. STEM EBIC and EELS acquisition

EELS and STEM EBIC images are acquired at the Lawrence Berkeley National Lab using the TEAM 1.0, which is equipped with a Gatan Continuum spectrometer and a K3 direct electron detector. Additional STEM EBIC imaging is performed on the Titan 80–300 S/TEM at UCLA. EELS spectrum images are acquired at a rate of 2.5 ms pixel^{-1} and a zero-loss peak full-width half-max of 0.7 eV. STEM EBIC images are acquired at a rate of 1.6–2.5 ms pixel^{-1} (100–200 s per frame). STEM EBIC is acquired using a NanoElectronic Imaging system with

an EBIC-optimized TEM sample holder by Hummingbird Scientific. STEM EBIC signals are acquired in parallel with the signals from other STEM imaging channels using the microscopes' native software.

2.3. Measurement procedure

PEET and STEM EBIC measurements are performed serially, rather than simultaneously, due to the dose limitations of the K3 direct electron detector used to acquire EELS. The heater is energized at various power values, in both bias polarities, while EELS spectrum images are acquired in regions near the electrode tips containing Al nanoparticles (figure 2). No dependence on the polarity of the heater bias is observed in the EELS measurements. Before subsequent STEM EBIC imaging, electrical testing is performed to confirm that the heater power at maximum bias equals that seen during the EELS maximum bias measurements to within 1% or better.

Following EELS, STEM EBIC is measured at regular heater power intervals. The power is generally stepped from highest power to lowest, but with repeats, reversed polarity, and zero-bias images to guard against dose effects and other systematic errors (Supplementary Data, figure S2). The region imaged with STEM EBIC (figure 2) contains the nanoparticles previously mapped with EELS during heater calibration. The beam is blanked prior to STEM EBIC acquisition to measure the beam-independent background current.

2.4. Data Analysis

For each EELS spectrum image, a temperature value at each pixel is calculated following the procedure described in reference [23]. Each temperature vs. heater power dataset is fit to a line with the intercept fixed at 295 K (figure 2 plot). The error bars in figure 2 are determined by setting the reduced $\chi^2 = 1$.

The STEM EBIC images are aligned and the beam-blanked signal is subtracted from the images to remove electronic offsets. The average signal in each of the red, green, and blue regions in figure 2 near the PEET-calibrated Al nanoparticle is converted to an amperage value. In the case of the a-C electrode device, the ∼100 nm-diameter Al nanoparticle used as a thermometer is free from residue and can be used as an additional material data point, with PEET and SEEBIC measurements taken from the same region. Each EBIC dataset is corrected (Supplementary Data, figure S2) for time-dependent systematics (e.g. drift in beam current) using the interspersed zero-bias measurements, and then for polarity-dependent attraction/repulsion of electrons caused by the heater bias (a few percent per volt, see Supplementary Materials for further discussion). In figure 3, the error bars in the Al and a-C data correspond to 50 fA, our approximate sensitivity under these imaging conditions [40, 41], while they correspond to 150 fA for the Pt data due to the greater variation in the large beam current used for those measurements.

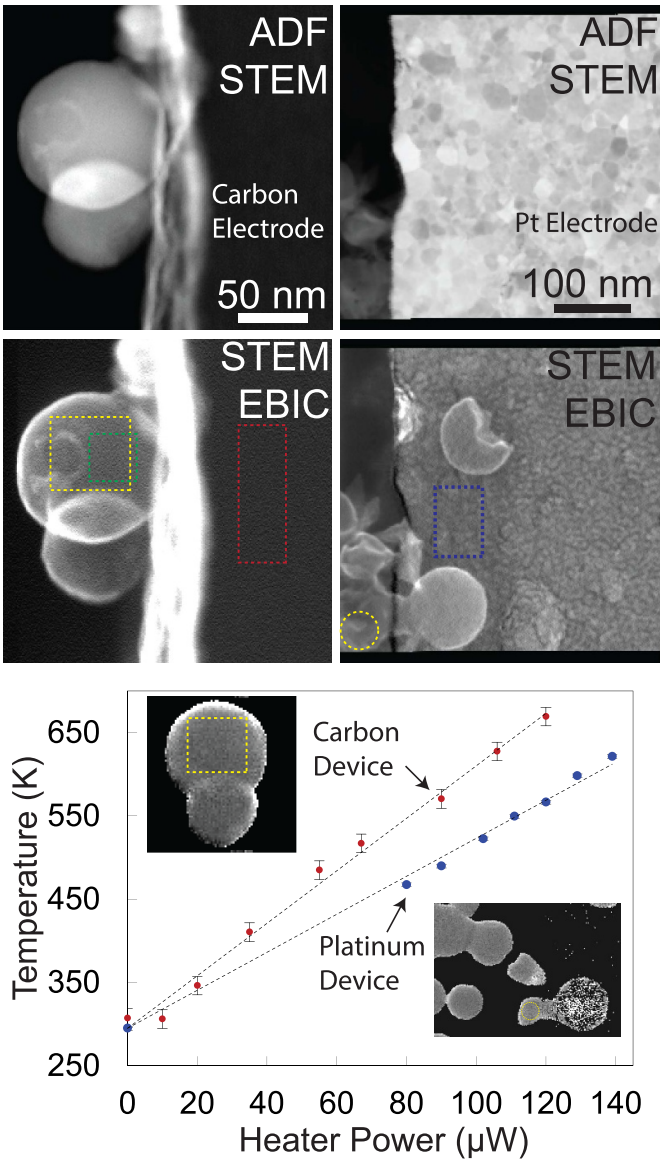

Figure 2. *(Upper rows)* ADF STEM and STEM EBIC images of the nanoparticle-decorated electrode tips from which EELS and STEM EBIC are measured for the data in figure 3. EBIC measurements in the figure 3 plots are the average signal in the green, red, and blue regions for Al, a-C, and Pt, respectively. The pixel size for the carbon and platinum device images are 0.9 nm and 1.7 nm, respectively. *(Lower row)* PEET-calibrated temperature as a function of heater power for each device. The plot's insets show representative EELS plasmon energy maps of each device. Yellow boxes in the EBIC and EELS images indicate the approximate location in which PEET temperature is measured for the figure 3 plots. The dashed lines in the plots show linear fits, with a fixed intercept of 295 K, for each PEET calibration dataset.

3. Results and discussion

We measure the EBIC from an aluminum nanoparticle, an amorphous carbon electrode, and (in a separate experiment) a platinum electrode, all as a function of temperature. In every case the temperature is determined via PEET measurements on an Al nanoparticle, as described above. Each dataset shows

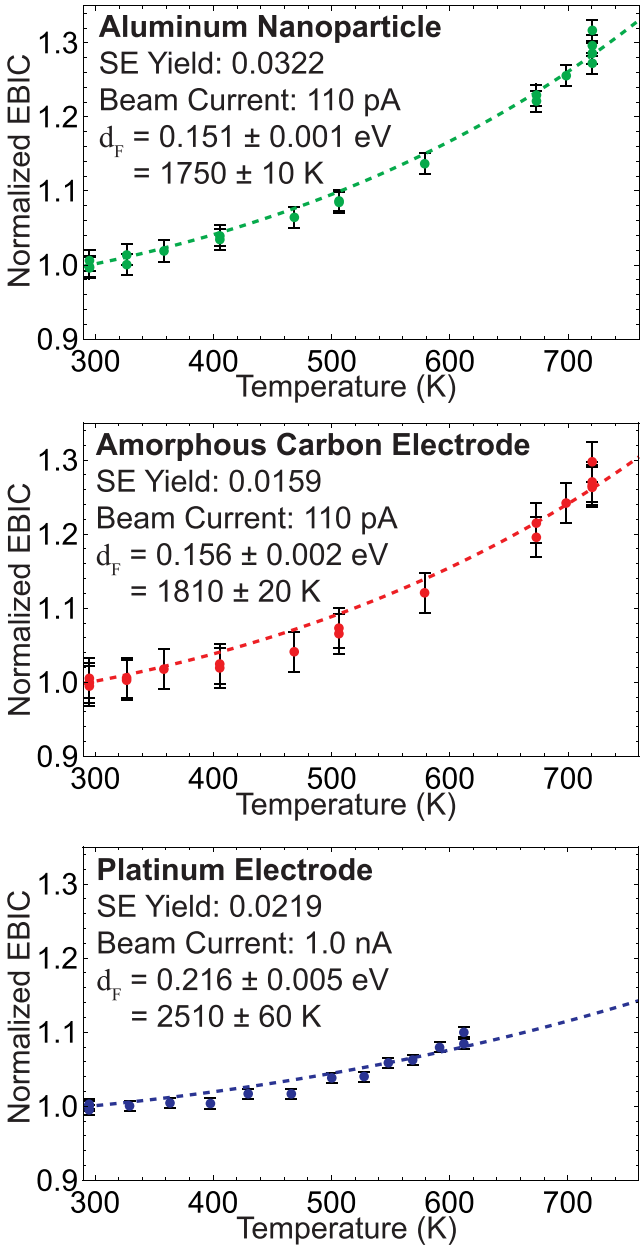

Figure 3. Average STEM EBIC signal from the regions indicated in figure 2 normalized to its room temperature value plotted as a function of PEET-calibrated temperature. The SE yield, beam current, and fit value for d_F are indicated for the data in each plot in units of electron volts and kelvins.

the SE emission increasing monotonically with temperature (figure 3). The change in EBIC for a given temperature change is largest for Al, slightly less for a-C, and smallest in Pt. The SE yield, or the SE emission current divided by the beam current, at room temperature is also shown for each material in figure 3. It should be noted that standard, detector-based SE imaging can only determine the relative magnitude of SE yields between materials, while SEEBIC enables precise SE yield measurements at each image pixel.

Under these conditions, the SE emission is not occurring at extremely high temperature (thermionic emission) nor at extremely high fields (field emission). Murphy and Good [19] used the free electron model to derive an expression for the temperature dependence of electron emission in this intermediate regime. Forbes [20] later refined and extended these results. Using Forbes' notation, the zero-temperature electron emission current density is scaled by a factor $\Theta(T)$ at finite temperature T, with the scaling factor given by:

$$\Theta(T) = \left(\frac{\pi k_B T}{d_F}\right) \frac{1}{\sin(\pi k_B T/d_F)} \tag{1}$$

where d_F is the decay width [20]. We define $\tilde{\Theta}(T) = \Theta(T)/\Theta(T_0)$, where $T_0 = 295$ K, which gives the temperature-dependent change in emission relative to room temperature. Each normalized EBIC dataset in figure 3 is fit to $\tilde{\Theta}(T)$ with d_F as the only free parameter, and the resulting fit value for d_F is indicated in each plot. Evaluating $\Theta(T_0)$ with the fitted values yields results between 1.02 and 1.05, within the typical room-temperature range 1.02–1.1 [20].

A strong and rapidly changing signal are desirable for more precise thermometry. Thus better thermometric materials will have larger SE yield and smaller decay widths d_F. Of the materials investigated here, aluminum looks to be the best and platinum the worst. For instance, at 600 K with a 1 nA electron beam and 50 fA EBIC sensitivity [40, 41], we would expect to achieve a precision of approximately 7, 5, and 2 K in Pt, C, and Al, respectively, (Supplementary Data, figure S3), with the potential for higher precision with longer integration.

As a practical example of SEEBIC thermometry, we map temperature in an un-calibrated Pt heater-electrode test structure. In this device, there are no Al nanoparticles (no EELS measured), and the heater and electrode are of a slightly different geometry than the figure 1 device (Supplementary Data, figure S5). The temperature map is generated using two EBIC images: one at room temperature, and one with heater power increasing from zero to 200 μW in 50 μW steps throughout the image (figure 4). For these images beam current is ~300 pA and frame time is 200 s. Thermally induced changes are obvious even in the raw EBIC image. Dividing the EBIC image with the heater powered by the heater-off image gives a map of normalized EBIC signal (or, equivalently, $\tilde{\Theta}(T)$). Using the approximation [20]:

$$\Theta(T) \approx 1 + (\pi k_B T/d_F)^2/6 \tag{2}$$

we derive an approximation for temperature as a function of the normalized EBIC signal, $\tilde{\Theta}$:

$$T\left(\tilde{\Theta}\right) = \sqrt{6\left(\frac{d_F}{\pi k_B}\right)^2\left(\tilde{\Theta}-1\right) + T_0^2\tilde{\Theta}}. \tag{3}$$

Using a value for d_F based on the Pt value in figure 3, but modified to compensate for bias asymmetry effects specific to this device (see discussion in the Supplementary Materials), equation (3) is used to perform simple image math on the normalized EBIC image to generate the corresponding temperature map (figure 4). The figure 4 temperature map has a gradient in time, vertically as heater

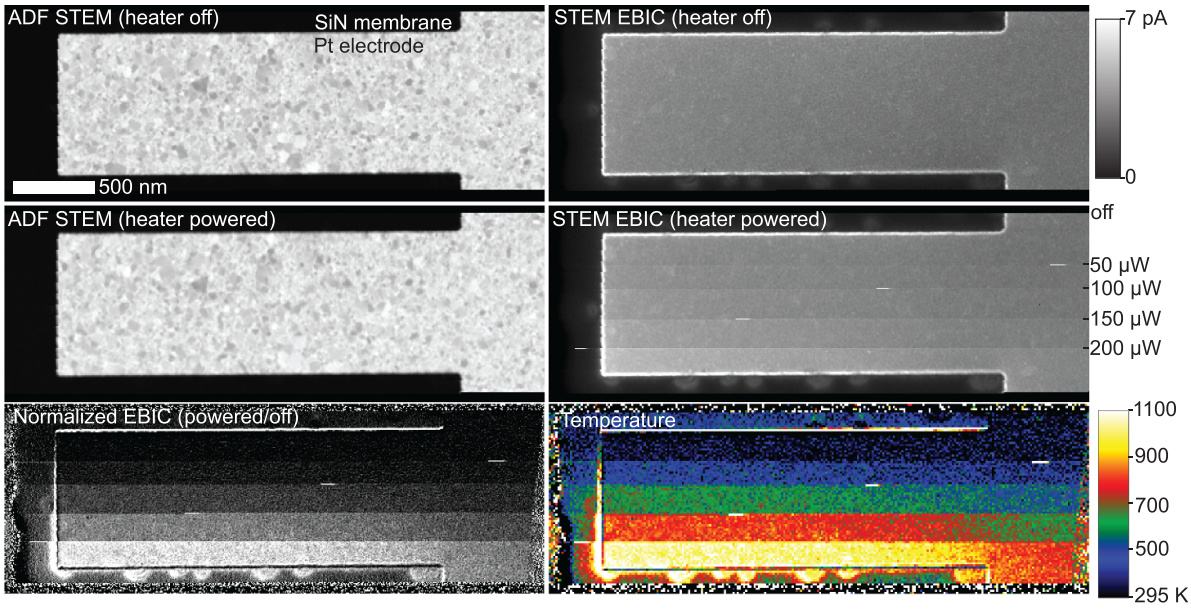

Figure 4. The ADF STEM and STEM EBIC images show an un-calibrated Pt heater-electrode structure with a slightly different geometry from the previous devices (Supplementary Data, figure S5). The device is shown with the heater off (*upper row*), and with the heater power increased during acquisition (*middle row*). White bands appear for a few pixels each time the voltage is changed. The heater-on image divided by the heater-off image generates a map of $\tilde{\Theta}(T)$ (*lower-left*), which, binned by two, is used to calculate the temperature map (*lower-right*).

power is increased, and in space, horizontally moving towards the right and away from the heater (see also Supplementary Data, figure S5). This device, with more robust heater leads, achieved much higher temperatures than the PEET-calibrated devices in figure 3. While the approximation in equation (2) simplifies image calculation, it deviates significantly from the original expression (equation (1)) at higher temperatures (by 3%–7% between 800 and 1100 K, see Supplementary Data, figure S6). Consequently, the higher temperature values in this map serve only as temperature estimates at present.

4. Conclusion

These results demonstrate that SEEBIC is a viable technique for mapping temperature in the TEM. Unlike its TEM-based predecessors, SEEBIC thermometry arises from a purely electronic measurement and is largely decoupled from physical considerations such as density, crystal structure, and strain. We did not investigate the resolution limits of SE thermometry below ∼1 nm. But because SE imaging (including SEEBIC) has been demonstrated at atomic resolution we expect that SEEBIC thermometry resolution surpasses the fundamental limitations for creating a nanoscale temperature gradient discussed in [23]. It remains to be seen whether similar results can be achieved with SE detection using a more conventional off-sample detector.

We obtain d_F values for SE emission from an Al nanoparticle and a-C and Pt thin films. However, these values for d_F are only relevant to these specific devices as the supporting Si_3N_4 membrane, and the Ti adhesion layer for the Pt, will likely impact SE emission from the bottom surface [4]. Measurements on suspended materials, perhaps in cross section, are necessary to determine intrinsic values of d_F. But, as pointed out by Forbes [20], with the appropriate correction factor determined numerically (for the SE-emission barrier in this case), d_F can be evaluated as a function of a material's work function. Determining this correction factor would extend SEEBIC thermometry to most non-insulating materials, as work function can also be measured with SEEBIC [4].

Data availability statement

The data cannot be made publicly available upon publication because they are not available in a format that is sufficiently accessible or reusable by other researchers. The data that support the findings of this study are available upon reasonable request from the authors.

Acknowledgments

This material is based upon work supported by the Defense Microelectronic Activity under Contracts HQ072720P0004 and HQ072721C0002, by National Science Foundation (NSF) Science and Technology Center (STC) Award DMR-1548924 (STROBE), and by NSF Award DMR-2004897. Imaging was performed at the Molecular Foundry at Lawrence Berkeley National Laboratory as well as at UCLA's California NanoSystems Institute (CNSI), where device fabrication was also performed. Work at the Molecular Foundry was supported by the Office of Science, Office of Basic Energy Sciences, of the U.S. Department of Energy under Contract No. DE-AC02-05CH11231.

References

[1] Reimer L. Scanning electron microscopy: physics of image formation and microanalysis. OCLC: 883383680

[2] Seiler H 1983 Secondary electron emission in the scanning electron microscope *J. Appl. Phys.* **54** R1–R18

[3] Egerton R F, Li P and Malac M 2004 Radiation damage in the TEM and SEM *Micron* **35** 399–409

[4] Hubbard W A, Mecklenburg M, Chan H L and Regan B C 2018 STEM imaging with beam-induced hole and secondary electron currents *Phys. Rev. Appl.* **10** 044066

[5] Kanter H 1961 Contribution of backscattered electrons to secondary electron formation *Phys. Rev.* **121** 681–4

[6] Zhu Y, Inada H, Nakamura K and Wall J 2009 Imaging single atoms using secondary electrons with an aberration-corrected electron microscope *Nat. Mater.* **8** 808–12

[7] Inada H, Su D, Egerton R F, Konno M, Wu L, Ciston J, Wall J and Zhu Y 2011 Atomic imaging using secondary electrons in a scanning transmission electron microscope: experimental observations and possible mechanisms *Ultramicroscopy* **111** 865–76

[8] Han M-G, Garlow J A, Marshall M S J, Tiano A L, Wong S S, Cheong S-W, Walker F J, Ahn C H and Zhu Y 2017 Electron-beam-induced-current and active secondary-electron voltage-contrast with aberration-corrected electron probes *Ultramicroscopy* **176** 80–85

[9] Mecklenburg M, Hubbard W A, Lodico J J and Regan B C 2019 Electron beam-induced current imaging with two-angstrom resolution *Ultramicroscopy* **207** 112852

[10] Dyck O, Swett J L, Evangeli C, Lupini A R, Mol J and Jesse S 2022 Contrast mechanisms in secondary electron e-beam-induced current (SEEBIC) imaging *Microsc. Microanal.* **28** 1567–83

[11] Everhart T E, Wells O C and Matta R K 1964 A novel method of semiconductor device measurements *Proc. IEEE* **52** 1642–7

[12] Dyck O, Almutlaq J, Lingerfelt D, Swett J L, Oxley M P, Huang B, Lupini A R, Englund D and Jesse S 2023 Direct imaging of electron density with a scanning transmission electron microscope *Nat. Commun.* **14** 7550

[13] Hubbard W A, Lingley Z, Theiss J, Sitzman S, Ayvazian T, Brodie M and Foran B 2019 Scanning transmission electron microscope mapping of electronic transport in polycrystalline $BaTiO_3$ ceramic capacitors *Appl. Phys. Lett.* **115** 133502

[14] Dyck O, Swett J L, Evangeli C, Lupini A R, Mol J A and Jesse S 2021 Mapping conductance and switching behavior of graphene devices in situ *Small Methods* **6** 2101245

[15] Hubbard W A, Lodico J J, Chan H L, Mecklenburg M and Regan B C 2022 Imaging dielectric breakdown in valence change memory *Adv. Funct. Mater.* **32** 2102313

[16] Vlasov E, Skorikov A, Sánchez-Iglesias A, Liz-Marzán L M, Verbeeck J and Bals S 2023 Secondary electron induced current in scanning transmission electron microscopy: an alternative way to visualize the morphology of nanoparticles *ACS Mater. Lett.* **5** 1916–21

[17] Vlasov E, Heyvaert W, Ni B, Van Gordon K, Girod R, Verbeeck J, Liz-Marzán L M and Bals S 2024 High-throughput morphological chirality quantification of twisted and wrinkled gold nanorods *ACS Nano* **18** 12010–9

[18] Evangeli C *et al* 2024 Thermoelectric limitations of graphene nanodevices at ultrahigh current densities *ACS Nano* **18** 11153–64

[19] Murphy E L and Good R H 1956 Thermionic emission, field emission and the transition region *Phys. Rev.* **102** 1464–73

[20] Forbes. R G 2004 Use of energy-space diagrams in free-electron models of field electron emission *Surf. Interface Anal.* **36** 395–401

[21] Khan M I, Lubner S D, Ogletree D F and Dames C 2018 Temperature dependence of secondary electron emission: a new route to nanoscale temperature measurement using scanning electron microscopy *J. Appl. Phys.* **124** 195104

[22] Zhang P 2023 The influence of sample temperature on SEM contrast of two types of nanostructures *Appl. Phys. A* **130** 37

[23] Mecklenburg M, Hubbard W A, White E R, Dhall R, Cronin S B, Aloni S and Regan B C 2015 Nanoscale temperature mapping in operating microelectronic devices *Science* **347** 629–32

[24] Idrobo J C, Lupini A R, Feng T, Unocic R R, Walden F S, Gardiner D S, Lovejoy T C, Dellby N, Pantelides S T and Krivanek O L 2018 Temperature measurement by a nanoscale electron probe using energy gain and loss spectroscopy *Phys. Rev. Lett.* **120** 095901

[25] Lagos M J and Batson P E 2018 Thermometry with subnanometer resolution in the electron microscope using the principle of detailed balancing *Nano Lett.* **18** 4556–63

[26] Wehmeyer G, Bustillo K C, Minor A M and Dames C 2018 Measuring temperature-dependent thermal diffuse scattering using scanning transmission electron microscopy *Appl. Phys. Lett.* **113** 253101

[27] Zhu M and Hwang J 2022 Scattering angle dependence of temperature susceptivity of electron scattering in scanning transmission electron microscopy *Ultramicroscopy* **232** 113419

[28] Barker A, Sapkota B, Oviedo J P and Klie R 2021 Automated plasmon peak fitting derived temperature mapping in a scanning transmission electron microscope *AIP Adv.* **11** 035330

[29] Chmielewski A, Ricolleau C, Alloyeau D, Wang G and Nelayah J 2020 Nanoscale temperature measurement during temperature controlled *in situ* TEM using Al plasmon nanothermometry *Ultramicroscopy* **209** 112881

[30] Kumar A, Tiukalova E, Venkatraman K, Lupini A, Hachtel J A and Chi M 2024 Calibrating cryogenic temperature of TEM specimens using EELS *Ultramicroscopy* **265** 114008

[31] Hubbard W A *et al* 2020 Electron-transparent thermoelectric coolers demonstrated with nanoparticle and condensation thermometry *ACS Nano* **14** 11510–7

[32] Mecklenburg M, Zutter B and Regan B C 2018 Thermometry of silicon nanoparticles *Phys. Rev. Appl.* **9** 014005

[33] Zutter B, Mecklenburg M and Regan B C 2016 Temperature dependence of the silicon nitride volume plasmon *Microsc. Microanal. Camb.* **22** 1574–5

[34] Hu X, Yasaei P, Jokisaari J, Öğüt S, Salehi-Khojin A and Klie R F 2018 Mapping thermal expansion coefficients in freestanding 2D materials at the nanometer scale *Phys. Rev. Lett.* **120** 055902

[35] Shen L, Mecklenburg M, Dhall R, Regan B C and Cronin S B 2019 Measuring nanoscale thermal gradients in suspended MoS2 with STEM-EELS *Appl. Phys. Lett.* **115** 153108

[36] Liao K, Shibata K and Mizoguchi T 2021 Nanoscale investigation of local thermal expansion at $SrTiO_3$ grain boundaries by electron energy loss spectroscopy *Nano Lett.* **21** 10416–22

[37] Cretu O, Tang D-M, Lu D-B, Da B, Nemoto Y, Kawamoto N, Mitome M, Ding Z and Kimoto K 2023 Nanometer-level temperature mapping of Joule-heated carbon nanotubes by plasmon spectroscopy *Carbon* **201** 1025–9

[38] Mecklenburg M, Zutter B T, Ling X Y, Hubbard W A and Regan B C 2021 Visualizing the electron wind force in the elastic regime *Nano Lett.* **21** 10172–7
[39] Yang Y-C, Serafini L, Gauquelin N, Verbeeck J and Jinschek J R 2025 Improving the accuracy of temperature measurement on TEM samples using plasmon energy expansion thermometry (PEET): addressing sample thickness effects *Ultramicroscopy* **270** 114102
[40] Hubbard W A, Mecklenburg M and Regan B C 2022 A low-noise, two-channel STEM EBIC metrology system *Microsc. Microanal.* **28** 794–5
[41] Bonifacio C S, Hubbard W, Li R, Ray M L and Fischione P 2024 TEM specimen preparation for STEM-EBIC analysis of advanced semiconductor devices *Microsc. Microanal.* **30** ozae044.066